Editors' Suggestion

Singular density correlations in chiral active fluids in three dimensions

Yuta Kuroda [1,2,*] Takeshi Kawasaki [1,3,4] and Kunimasa Miyazaki [1]

[1]*Department of Physics, Nagoya University, Nagoya 464-8602, Japan*

[2]*Institute for Theoretical Physics IV, University of Stuttgart, Heisenbergstrasse 3, 70569 Stuttgart, Germany*

[3]*D3 Center, The University of Osaka, Toyonaka, Osaka 560-0043, Japan*

[4]*Department of Physics, The University of Osaka, Toyonaka, Osaka 560-0043, Japan*

(Received 13 July 2025; accepted 30 September 2025; published 27 October 2025)

We investigate density fluctuations in three-dimensional chiral active fluids by using a simple model of helical self-propelled particles. Helical motion is generated by a constant angular velocity (or chiral torque) acting on the self-propelled force. The chiral torque is assumed to have the same direction and magnitude for all particles. Due to the helical nature of the particle motion, the system is generically anisotropic even when it is spatially homogeneous. Numerical simulations demonstrate that the helicity induces an anisotropic pattern and a singularity in the static structure factor (the density correlation function in Fourier space) in the low-wave-number limit. Moreover, the system in the limit of infinite persistence time exhibits hyperuniformity in the direction perpendicular to the chiral torque, while giant density fluctuations emerge along the parallel direction. We then construct a fluctuating hydrodynamic theory for the system to describe the singular behavior. A linear analysis of the resulting equations yields an analytical expression for the static structure factor, which qualitatively agrees with our numerical findings.

DOI: 10.1103/25s2-6y3m

I. INTRODUCTION

Self-propelled particles have been widely used to model active matter and have revealed numerous novel phenomena arising from their nonequilibrium nature [1–3]. Among various types of self-propelled particles, chiral self-propelled particles, whose motions violate mirror symmetry, have recently attracted significant attention [4,5]. In two dimensions, they typically exhibit circular trajectories. Experimental realizations of such chiral self-propelling motions include asymmetric-shaped colloidal objects [6,7], Janus particles with an asymmetric coating [8], sperm cells [9], malaria parasites [10], bacteria swimming near walls or surfaces [11,12], and light-driven walkers [13]. In numerical simulations, such circular motion is often modeled by introducing chirality into active Brownian particles (ABP) [4,5]. It has been reported that the chiral motions of constituents give rise to collective phenomena that are not observed in nonchiral counterparts. Examples include the formation of vortices [14–17], absorbing phase transition [18], reentrant behavior of glassy slow dynamics [19], anomalous two-dimensional crystallization [20,21], Hall-like currents [22], and self-reverting vorticity of clusters [23]. In addition to chiral self-propelled particles, active spinner systems, where particles rotate but do not self-propel, have also been studied intensively [5,24–26].

In addition to the aforementioned examples, one of the most striking features of two-dimensional chiral self-propelled particles is the suppression of long-wavelength density fluctuations [18,27–29]. This phenomenon is known as hyperuniformity [30,31]. Hyperuniformity is characterized by the vanishing of the static structure factor $S(q)$ in the small-wave-number limit, with q denoting the wavenumber. In most cases, the asymptotic behavior is a power law as $S(q \to 0) \sim q^{\alpha}$ with $\alpha > 0$. This feature is in contrast to nonchiral active fluids, which typically exhibit enhancement of density fluctuations (also known as giant number fluctuations, GNF) [32–40]. Hyperuniformity has been observed in a variety of nonequilibrium dynamical systems [31], such as periodically driven colloidal suspensions near absorbing transition points [41–43], center-of-mass-conserving systems [44–48], granular systems [48–50], nonreciprocal active robotic systems in chiral states [51], epithelial tissues with pulsating synchronization [52], deterministic antialigning polar active fluids [53], and the late-stages of spinodal decomposition described by the Cahn-Hilliard equation [54] and its active counterpart (active model B without noise) [55].

While most studies focused on two-dimensional systems, three-dimensional chiral active particles, whose motion becomes helical, are also of great interest. Examples of such systems include sperm cells [56], choanoflagellates [57], and nematic liquid crystal droplets in surfactant solutions [58,59], all of which are known to exhibit helical trajectories. Theoretically, the single-particle dynamics of three-dimensional extensions of chiral active Brownian particles [60,61], as well as of helical swimmers driven by hydrodynamic interactions with the surrounding fluid [62–64], have been investigated. Yet, the collective behavior arising from helical motion has received relatively little attention, with the exception of a study on hydrodynamically interacting helical swimmers [65].

In this paper, we study density fluctuations in a collection of helical active swimmers using a simple particle model. Helicity is introduced by adding a constant angular velocity (or torque) to the equation of motion for the self-propulsion in three-dimensional ABP, following the

*Contact author: yuta.kuroda@itp4.uni-stuttgart.de

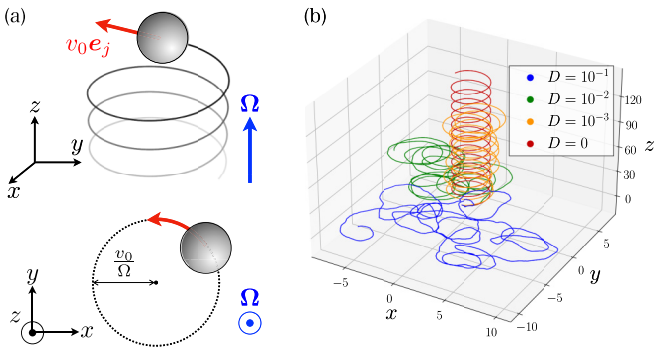

FIG. 1. (a) Schematic illustration of the model of a helical self-propelled particle. The illustration shows the case of $\boldsymbol{\Omega} = (0, 0, \Omega)$ and zero noise. The top panel depicts the motion in three dimensions, and the bottom panel shows its projection onto the x-y plane. (b) Typical trajectories of a single free particle for various rotational diffusion constants. The chiral torque is fixed as $\boldsymbol{\Omega} = (0, 0, \Omega)$ with $\Omega = 0.4$. Time is measured in units of $\tau = \sigma/v_0$.

approach in Refs. [60,61]. In this model, the key parameters are the magnitude of the torque and the persistence time (or the rotational diffusion constant). Each particle exhibits helical motion along the direction of the torque vector, resulting in anisotropic dynamics. The torque vector is assumed to be aligned in the same direction for all particles. We perform extensive numerical simulations in the homogeneous fluid states and find that the density correlation function exhibits a singular behavior, characterized by a discontinuity in the low-wavenumber limit of the static structure factor. In addition, we observe an anisotropic pattern in the static structure factor. These properties are akin to those observed in other anisotropic nonequilibrium fluids, such as active particles with anisotropic self-propulsion [66–68] and in driven diffusive gases [69,70]. In our system, density fluctuations are enhanced along the direction of the torque, while they are suppressed in the perpendicular directions. In particular, in the limit of infinite persistence time, the system exhibits hyperuniformity in the directions perpendicular to the torque. To understand these numerical observations, we construct a fluctuating hydrodynamic theory by a bottom-up approach and analytically calculate the static structure factor. The resulting expression qualitatively captures the observed behaviors in the numerical simulation, although some quantitative discrepancies remain.

This paper is organized as follows. In Sec. II, we present the details of the particle-based model for helical active swimmers. Section III provides numerical results for the density fluctuations in the homogeneous fluid states. To explain the qualitative features observed in the simulations, we develop a fluctuating hydrodynamic theory in Sec. IV, and derive an analytical expression for the density correlation function via linear analysis. Finally, Sec. V summarizes our results.

II. MODEL

We study a model of helical self-propelled particles [60], which we here refer to as three-dimensional (3D) cABP, illustrated in Fig. 1(a). The equation for the position of the jth particle is given by

$$\frac{\mathrm{d}\boldsymbol{r}_j(t)}{\mathrm{d}t} = \mu \boldsymbol{F}_j(t) + v_0 \boldsymbol{e}_j(t), \tag{1}$$

where μ and v_0 stand for the mobility and the constant self-propulsion speed, respectively. The interaction force acting on the jth particle is given by $\boldsymbol{F}_j(t) = -\sum_{k(\neq j)} \nabla_j U(|\boldsymbol{r}_j - \boldsymbol{r}_k|)$, where $U(r)$ is a short-range pairwise potential. $\boldsymbol{e}_j = (e_j^{(x)}, e_j^{(y)}, e_j^{(z)})$ is a three-dimensional unit vector and represents the direction of the self-propelled motion. This unit vector can also be expressed by two polar angles, ϕ_j with respect to the x axis (the azimuthal angle) and θ_j with respect to the z axis (the zenith angle), as $\boldsymbol{e}_j = (\sin\theta_j \cos\phi_j, \sin\theta_j \sin\phi_j, \cos\theta_j)$. We assume the time evolution of the unit vector $\boldsymbol{e}_j(t)$ to obey

$$\frac{\mathrm{d}\boldsymbol{e}_j(t)}{\mathrm{d}t} = (\boldsymbol{\Omega} + \sqrt{2D}\boldsymbol{\eta}_j(t)) \overset{\mathrm{s}}{\times} \boldsymbol{e}_j(t). \tag{2}$$

Here, D denotes the rotational diffusion constant. The persistent time in three dimensions is given by $\tau_\mathrm{p} = 1/(2D)$. The vector $\boldsymbol{\Omega}$ is a constant torque that generates helical motions. The unit vector $\boldsymbol{e}_j(t)$ is subjected to a Gaussian white noise $\boldsymbol{\eta}_j(t)$ with zero mean and the correlation $\langle \eta_j^{(\alpha)}(t) \eta_k^{(\beta)}(t') \rangle = \delta_{j,k}\delta_{\alpha,\beta}\delta(t - t')$, where the symbol $\langle \cdots \rangle$ denotes the ensemble average and the Greek indices denote Cartesian coordinates $\alpha, \beta \in \{x, y, z\}$. Note that the cross product in Eq. (2), $\overset{\mathrm{s}}{\times}$, is taken in the Stratonovich representation [71]. This model is a simple extension of two-dimensional chiral active Brownian particles [18,19,72,73] to a three-dimensional case. In the limit $\boldsymbol{\Omega} \to \boldsymbol{0}$ at finite D, Eqs. (1) and (2) reduce to active Brownian spheres or three-dimensional ABP [74–77]. We remark that, in reality, each helical swimmer likely has a different direction and magnitude of the torque. However, to focus on the effects of helical motion on density fluctuations, we consider a simple situation in which all particles are driven by the same constant torque $\boldsymbol{\Omega}$.

Figure 1(b) shows the typical trajectories of a single free particle for several values of D, with time measured in units of $\tau = \sigma/v_0$, where σ is the particle diameter. The torque vector $\boldsymbol{\Omega}$ is oriented along the z axis $\boldsymbol{\Omega} = (0, 0, \Omega)$. When D is very small, the trajectory becomes helical along the direction of $\boldsymbol{\Omega}$, provided that the z component of the orientational vector $\boldsymbol{e}_j(t)$ is nonzero. In the noiseless case ($D = 0$), the particle performs a perfect helical motion. As D increases, the trajectories become more stochastic and the influence of chirality becomes less pronounced. The single-particle dynamics of 3D cABP wre characterized in Refs. [60,61], based on mean-square displacement and higher-order moments.

III. NUMERICAL SIMULATION

A. Setup

We numerically simulate a system of N interacting particles, governed by Eqs. (1) and (2), in a cubic box of side length L with periodic boundary conditions. The details of the simulation setup are as follows. We numerically integrate the equation for the orientation, Eq. (2), by the Euler-Maruyama method. The vector $\boldsymbol{e}_j(t)$ is normalized after each time step to ensure that the magnitude is unity. For the pairwise

interaction, we consider only a short-range repulsive force, as in previous studies of the two-dimensional case [18,72,73]. To this end, we employ the Weeks-Chandler-Andersen (WCA) potential given by [78]

$$U(r) = 4\epsilon\left[\left(\frac{\sigma}{r}\right)^{12} - \left(\frac{\sigma}{r}\right)^{6} + \frac{1}{4}\right] \tag{3}$$

for $r < 2^{1/6}\sigma$ and $U(r) = 0$ otherwise. Here, σ is the diameter of a particle and $2^{1/6}\sigma$ is the cutoff length. The units of length and time are chosen as σ and $\tau = \sigma/v_0$, respectively. Unless otherwise noted, all parameters are expressed in these units; that is, we set $\sigma = 1$ and $v_0 = 1$. The time step is set to $\Delta t = 10^{-3}$, and the number of particles is $N = 8\times10^4$. Without loss of generality, we align the torque vector $\boldsymbol{\Omega}$ with the z axis. The control parameters are the mean number density ρ, the rotational diffusion constant D, the orbital radius $R = v_0/\Omega$, and the dimensionless energy ratio $\mu\epsilon/(\sigma v_0)$. Throughout this section, we focus on a low-density $\rho = 0.5$ [corresponding to a packing fraction of $N\pi\sigma^3/(6L^3) \simeq 0.26$], and we fix the parameter $\mu\epsilon/(\sigma v_0) = 1/24$. We compute the static structure factor $S(\boldsymbol{q}) = \langle\sum_{j,k=1}^{N} e^{-i\boldsymbol{q}\cdot(\boldsymbol{r}_j-\boldsymbol{r}_k)}\rangle/N$ after confirming that the system has reached a stationary state by monitoring the time evolution of the potential energy. We also verify that the system remains homogeneous and does not exhibit clustering or phase separation for any of the parameter sets used in this study, whereas the ABP model without chirality is known to undergo motility-induced phase separation (MIPS) even in three dimensions [74–77]. The effects of chirality on MIPS in three dimensions are beyond the scope of the present study.

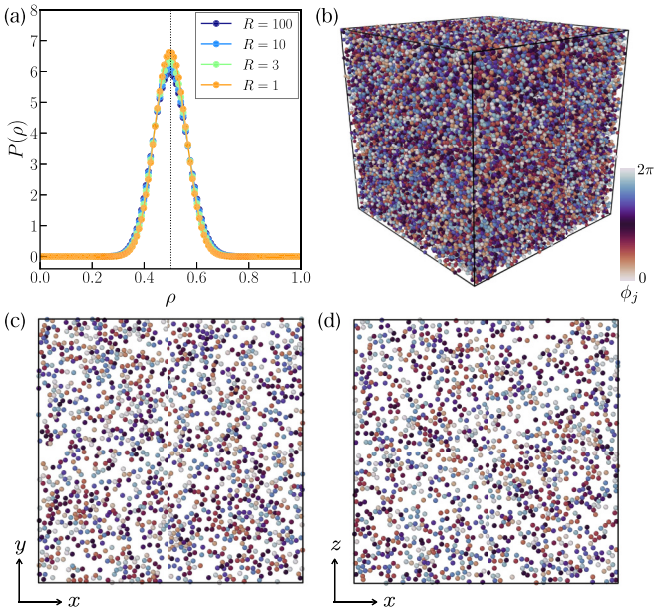

FIG. 2. (a) The local density distribution $P(\rho)$ at $D = 0$. In this figure, ρ denotes the local density. The vertical dotted line indicates the mean density $\rho = 0.5$. (b) A typical particle configuration in the steady state at $D = 0$, $\rho = 0.5$, and $R = 1$. The color represents the azimuthal angle ϕ_j of the orientation vector $\boldsymbol{e}_j$, defined as $\boldsymbol{e}_j = (\sin\theta_j\cos\phi_j, \sin\theta_j\sin\phi_j, \cos\theta_j)$, where θ_j is the zenith angle. Cross-sectional particle configurations with thickness σ in (c) the x-y plane at $z = L/2$ and (d) the x-z plane at $y = L/2$.

B. Results

We first consider the noiseless limit ($D = 0$), in which a free particle exhibits a perfect helical motion. Figure 2(a) shows the local density distribution $P(\rho)$ for $D = 0$. Here, we calculate the local density by averaging the number of particles within small spherical regions of radius 3σ. For all values of R, the distribution is unimodal with a peak at the mean density, indicating that the system remains homogeneous. Figure 2(b) presents a representative snapshot of the simulation at $D = 0$, where the color positions the azimuthal angle ϕ_j of the orientation vector $\boldsymbol{e}_j$. We also present sliced snapshots of the particle configurations in the x-y and x-z planes, shown in Figs. 2(c) and 2(d), respectively. The particle positions and orientations are randomly distributed, and the system exhibits no characteristic structures such as clustering or synchronization.

We now observe the static structure factor $S(\boldsymbol{q})$. Note that $S(\boldsymbol{q})$ cannot be reduced to a function of the scalar variable $q = |\boldsymbol{q}|$ as $S(q)$ because the system is not invariant under rotations about the x or y axes.

In Figs. 3(a) and 3(c), we show the static structure factor at $R = 1$ in the q_x-q_z plane and in the q_x-q_y plane, respectively. Reflecting the anisotropy of the system, the static structure factor in the q_x-q_z plane exhibits an anisotropic pattern, whereas it remains isotropic in the q_x-q_y plane. To examine this anisotropy in more detail, we plot $S(0, 0, q_z)$ and $S(q_x, 0, 0)$ in Figs. 4(a) and 4(b), respectively. On the

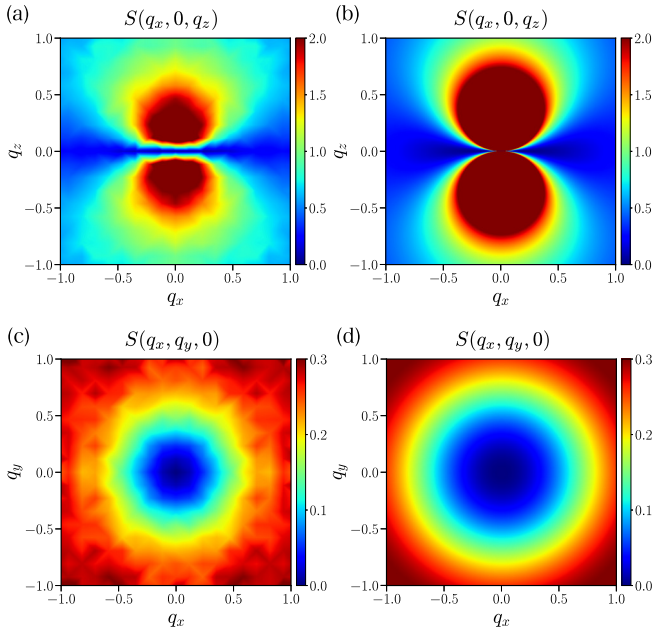

FIG. 3. Contour plots of the static structure factor $S(\boldsymbol{q})$ at $D = 0$ and $R = 1$ (or $\Omega = 1$). The upper panels show $S(\boldsymbol{q})$ in the q_x-q_z plane obtained from (a) numerical simulations and (b) theoretical analysis. The lower panels show $S(\boldsymbol{q})$ in the q_x-q_y plane obtained from (c) numerical simulations and (d) theoretical analysis.

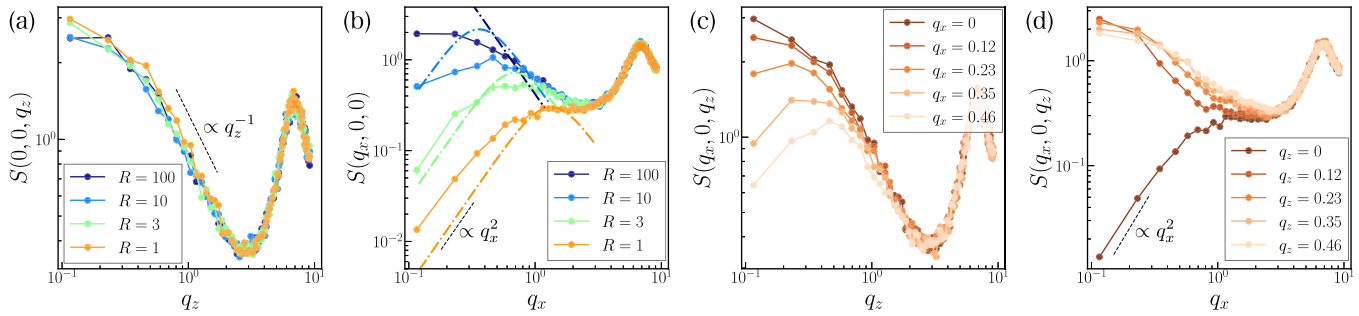

FIG. 4. The static structure factor $S(\boldsymbol{q})$ obtained from the numerical simulation at $D = 0$ on (a) the q_z axis and (b) the q_x axis. The dashed-dotted lines in (b) represent the predictions of the linearized theory. (c) and (d) show the static structure factor $S(\boldsymbol{q})$ in the q_x-q_z plane at $R = 1$ and $D = 0$. (c) $S(q_x, 0, q_z)$ as a function of q_z for various q_x. (d) $S(q_x, 0, q_z)$ as a function of q_x for various q_z.

q_z axis, $S(\boldsymbol{q})$ is enhanced at small q_z and is insensitive to R or chirality Ω, which is natural since the z-component of Eq. (2) does not depend on Ω. In contrast, $S(\boldsymbol{q})$ on the q_x axis appears to vanish in the limit $q_x \to 0$, i.e., hyperuniformity with the exponent $\alpha = 2$ is observed. Although hyperuniformity is not evident for large radii, $R = 100$ and 10, it is expected that $S(q_x, 0, 0)$ eventually goes to zero with the same hyperuniform exponent if the system size is sufficiently large. These observations indicate that the static structure factor in this system is singular at the origin of Fourier space: $\lim_{q_z\to 0} S(0, 0, q_z) \neq \lim_{q_x\to 0} S(q_x, 0, 0)$. Since the system is isotropic in the x-y plane, more generally, $\lim_{q_z\to 0} S(0, 0, q_z) \neq \lim_{q\to 0} S(q_x, q_y, 0)$. We also show the behavior of the static structure factor $S(q_x, 0, q_z)$ as a function of q_z and q_x with fixed $q_x, q_z(\geqslant 0)$ in Figs. 4(c) and 4(d). In Fig. 4(c), we observe that increasing q_x leads to suppression of $S(q_x, 0, q_z)$ as a function of q_z in the small-wave-number regime. In other words, $S(q_x, 0, q_z)$ is maximized at $q_x = 0$, which is also evident in Fig. 3(a). $S(q_x, 0, q_z)$ as a function of q_x, shown in Fig. 4(d), exhibits hyperuniformity only at $q_z = 0$, while for $q_z > 0$, the density fluctuations are instead enhanced.

Anisotropic patterns and singularities in the static structure factor have also been observed in other anisotropic nonequilibrium systems. In Ref. [67], the authors studied active Brownian particles with anisotropic self-propulsion in two dimensions and reported singular density correlations in the homogeneous fluid phase. Lattice models of active fluids with spatial anisotropy are also known to exhibit similar features in density correlations, as shown by numerical simulations and field-theoretical analysis [66,68]. In addition, passive anisotropic systems driven out of equilibrium, such as randomly driven diffusive gases, have long been known to exhibit singular density correlations [69,70]. The anisotropic pattern of $S(\boldsymbol{q})$ in these systems is referred to as the "butterfly" or "owl" pattern [70]. These observations suggest that the anisotropic pattern and singularity of $S(\boldsymbol{q})$ are robust features of anisotropic nonequilibrium fluids. However, our system differs from the above examples in that the density fluctuations are hyperuniform in the plane perpendicular to the torque vector $\boldsymbol{\Omega}$. Such anisotropic hyperuniform states were previously proposed in Ref. [79], and our system can be regarded as a concrete realization of this concept.

Qualitatively, the singular behavior of the density correlation in the system can be understood from established properties of standard ABP and cABP in two dimensions. First, in the fluid phase of standard ABP, it is known that spatial velocity correlations develop [80,81], and concomitantly, long-wavelength density fluctuations are enhanced [82,83]. These density fluctuations possess a finite correlation length given by $\xi \propto \sqrt{1/D}$ and become long-ranged in the limit $D = 0$ or infinite persistence time [82,83]. Second, two-dimensional cABP systems are known to exhibit hyperuniformity, characterized by the exponent $\alpha = 2$, as confirmed by both numerical simulations [18] and theoretical analysis [29]. Since the particle motion in our model can be effectively regarded as "one-dimensional ABP" along the z axis and two-dimensional cABP in the x-y plane, it is natural that $S(0, 0, q_z)$ exhibits enhancement, whereas $S(q_x, q_y, 0)$ displays hyperuniformity. We finally examine the effect of the rotational diffusion constant D (or the persistence time) on the density correlation function. Figure 5(a) shows the static structure factor along the q_z axis, $S(0, 0, q_z)$, for several values of D at $R = 1$. As D increases, the intensity of $S(0, 0, q_z)$ at small q_z decreases. This trend is consistent with the fact that our model approaches equilibrium in the limit $D \to \infty$. In Fig. 5(b), we show the static structure factor along the q_x axis, $S(q_x, 0, 0)$, for various values of D. As D increases, the hyperuniform behavior appears to vanish. Although we cannot definitively conclude the disappearance of hyperuniformity for finite D due to the limited system size, it is natural to infer that $S(q_x \to 0, 0, 0)$ remains nonzero for $D \neq 0$, similar

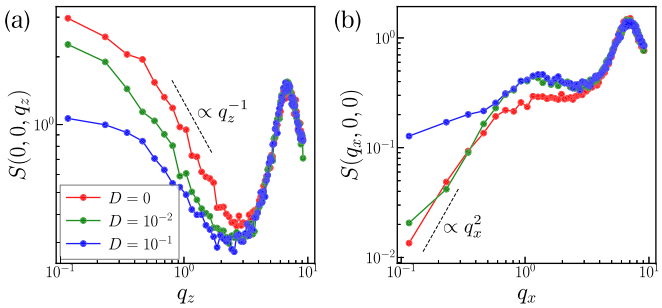

FIG. 5. Static structure factor obtained from the numerical simulation at $\rho = 0.5$ and $R = 1$. Panels (a) and (b) show the static structure factor on the q_z and q_x axis for various D, respectively. In panel (a), the black dashed line represents q_z^{-1} as a guide for the eye. The black dashed line in panel (b) is proportional to q_x^2.

to the case of two-dimensional cABP, which exhibit perfect hyperuniformity only when $D = 0$ [18,29]. Furthermore, by comparing the numerical values of $S(0, 0, q_z)$ and $S(q_x, 0, 0)$ at the smallest wave number, we find that the density correlation remains singular even at finite D.

IV. THEORY

To understand the numerical results presented in the previous section, we develop a fluctuating hydrodynamic theory for the homogeneous fluid state of 3D cABP and calculate the static structure factor through linear analysis.

A. Fluctuating hydrodynamic equations

Our interest lies in long-wavelength density fluctuations. To analyze such large-scale behavior of the density field, hydrodynamic descriptions provide a standard theoretical tool. Several approaches have been proposed to derive hydrodynamic equations for active particle models. A prevalent method involves deriving equations for the average density and polarization by reducing the Fokker-Planck equation to an effective one-body equation and applying closure approximations [84–86]. This approach has also been applied to chiral active particles in two dimensions to investigate instabilities [18,73,87–89]. Another approach is based on kinetic theories for active matter, which has recently been considered for chiral active particles [90]. However, in these approaches, noise terms must be added by hand when one wants to describe fluctuations of hydrodynamic variables [91,92]. To address fluctuations, we adopt Dean's method [93–95], which enables the derivation of hydrodynamic equations with noise terms. In the case of two-dimensional cABP, this method successfully reproduces hyperuniformity with the same exponent as observed in numerical simulations, although discrepancies remain in the amplitude of the density correlation function [29].

The field variables that we consider are the density field and polarization, defined by

$$\rho(\boldsymbol{r}, t) = \sum_{j=1}^{N} \delta[\boldsymbol{r} - \boldsymbol{r}_j(t)], \tag{4}$$

$$\boldsymbol{p}(\boldsymbol{r}, t) = \sum_{j=1}^{N} \boldsymbol{e}_j(t)\delta[\boldsymbol{r} - \boldsymbol{r}_j(t)], \tag{5}$$

respectively. By employing Dean's method [93,94], one can find the following set of equations for the density field $\rho(\boldsymbol{r}, t)$ and the polarization $\boldsymbol{p}(\boldsymbol{r}, t)$ (see Appendix for the derivation):

$$\partial_t \rho(\boldsymbol{r}, t) = -\nabla \cdot \boldsymbol{J}(\boldsymbol{r}, t), \tag{6}$$

$$\boldsymbol{J}(\boldsymbol{r}, t) = -\mu \nabla \cdot \mathsf{P}(\boldsymbol{r}, t) + v_0 \boldsymbol{p}(\boldsymbol{r}, t), \tag{7}$$

$$\partial_t \boldsymbol{p}(\boldsymbol{r}, t) = -\nabla \cdot \left(\frac{\boldsymbol{J}(\boldsymbol{r}, t)\boldsymbol{p}(\boldsymbol{r}, t)}{\rho(\boldsymbol{r}, t)} \right) - 2D\boldsymbol{p}(\boldsymbol{r}, t) + \boldsymbol{\Omega} \times \boldsymbol{p}(\boldsymbol{r}, t) + \sqrt{\frac{4D\rho(\boldsymbol{r}, t)}{3}} \boldsymbol{\Upsilon}(\boldsymbol{r}, t), \tag{8}$$

where the first term on the right-hand side (RHS) of Eq. (7) is the "pressure" tensor defined as

$$\nabla \cdot \mathsf{P}(\boldsymbol{r}) = \rho(\boldsymbol{r}) \nabla \frac{\delta \mathcal{F}[\rho(\cdot)]}{\delta \rho(\boldsymbol{r})} \tag{9}$$

with

$$\mathcal{F}[\rho(\cdot)] = \frac{1}{2} \int_V \mathrm{d}^3\boldsymbol{r} \int_V \mathrm{d}^3\boldsymbol{r}' \, \rho(\boldsymbol{r})\rho(\boldsymbol{r}')U(|\boldsymbol{r} - \boldsymbol{r}'|). \tag{10}$$

The explicit form of the pressure tensor in terms of the density field and the pair interaction is given by the Irving-Kirkwood formula [96,97], but we do not need it in the following discussion. $\boldsymbol{\Upsilon}(\boldsymbol{r}, t)$ in Eq. (8) is a Gaussian white noise with zero mean $\langle \Upsilon_\alpha(\boldsymbol{r}, t) \rangle = 0$ and the correlation $\langle \Upsilon_\alpha(\boldsymbol{r}, t)\Upsilon_\beta(\boldsymbol{r}', t') \rangle = \delta_{\alpha,\beta}\delta(\boldsymbol{r} - \boldsymbol{r}')\delta(t - t')$. Equations (6) to (8) have the same form as that in the two-dimensional case [29] except for the coefficients in Eq. (8). We remark that Eqs. (6) to (8) reduce to the Dean-Kawasaki equation for overdamped equilibrium systems in the limit $D \to 0$ with $T_{\mathrm{act}} = v_0^2/(6D\mu)$ being constant [29].

Equations (6) to (8), derived via an extended Dean's method, are rigorous except for an assumption that each particle does not occupy the same position simultaneously (see Appendix). Therefore, Eqs. (6) to (8) have the same information as the original equations, Eqs. (1) and (2). We henceforth focus on the large-scale or low-wave-number limit. Since in homogeneous fluid states at the coarse-grained scales, one expects higher-order terms in gradients and in density fluctuations to be negligible, one assumes that the pressure gradient can be written as

$$\nabla \cdot \mathsf{P}(\boldsymbol{r}) \simeq \frac{1}{\rho\chi} \nabla \delta\rho(\boldsymbol{r}), \tag{11}$$

where the coefficient χ is defined by $\chi^{-1} = \rho \partial P/\partial\rho|_{\rho(\boldsymbol{r})=\rho}$ with $P(\boldsymbol{r}) = \mathrm{Tr}[\mathsf{P}(\boldsymbol{r})]/3$. Although this assumption is crude, it is enough to capture the qualitative behavior of the density correlation function, as we will see below. If we wish to study instabilities or nonlinear effects, the pressure tensor needs to be further expanded to higher-order terms in ρ and $\boldsymbol{p}$ [92], but it is outside the scope of the present study. Together with the assumption, Eq. (11), and the linearization of equations around the homogeneous solutions, we have

$$\partial_t \delta\rho(\boldsymbol{r}, t) = b\nabla^2 \delta\rho(\boldsymbol{r}, t) - v_0 \nabla \cdot \delta\boldsymbol{p}(\boldsymbol{r}, t), \tag{12}$$

$$\partial_t \delta\boldsymbol{p}(\boldsymbol{r}, t) = -2D\delta\boldsymbol{p}(\boldsymbol{r}, t) + \boldsymbol{\Omega} \times \delta\boldsymbol{p}(\boldsymbol{r}, t) + \sqrt{\frac{4D\rho}{3}} \boldsymbol{\Upsilon}(\boldsymbol{r}, t), \tag{13}$$

where we define $b := \mu/(\rho\chi)$.

Before looking at the density correlation function, we remark on the equilibrium limit of the linearized equations, Eqs. (12) and (13). Since Eq. (13) is closed for the polarization, $\boldsymbol{\xi}(\boldsymbol{r}, t) := v_0 \delta\boldsymbol{p}(\boldsymbol{r}, t)$ can be regarded as a colored noise. This colored noise $\boldsymbol{\xi}(\boldsymbol{r}, t)$ has zero mean and the correlation

$$\langle \boldsymbol{\xi}(\boldsymbol{r}, t)\boldsymbol{\xi}^{\mathrm{T}}(\boldsymbol{r}', t') \rangle = \frac{v_0^2 \rho}{3} \mathsf{R}_{\boldsymbol{\Omega}}[\Omega(t - t')] e^{-2D|t-t'|} \delta(\boldsymbol{r} - \boldsymbol{r}'), \tag{14}$$

where T denotes the transpose. $\mathsf{R}_{\boldsymbol{\Omega}}(\theta)$ in Eq. (14) is the rotation matrix representing a rotation by an angle θ around

the vector $\boldsymbol{\Omega}$, given by the Rodrigues' formula:

$$\mathsf{R}_{\boldsymbol{\Omega}}(\theta) = e^{\theta \mathsf{K}(\boldsymbol{\Omega})}, \quad K_{\alpha,\beta}(\boldsymbol{\Omega}) = \frac{1}{\Omega} \sum_{\mu\in\{x,y,z\}} \epsilon_{\alpha\mu\beta}\Omega_\mu, \tag{15}$$

where $\Omega = |\boldsymbol{\Omega}|$ and $\epsilon_{\alpha\beta\gamma}$ is the Levi-Civita tensor. In the limit $D \to \infty$ while keeping $T_{\rm act} = v_0^2/(6D\mu)$ constant, Eq. (14) becomes a Gaussian white noise and the fluctuation-dissipation relation is recovered

$$\langle \boldsymbol{\xi}(\boldsymbol{r}, t)\boldsymbol{\xi}^{\rm T}(\boldsymbol{r}', t')\rangle = 2\mu T_{\rm act}\rho\delta(t-t')\delta(\boldsymbol{r}-\boldsymbol{r}')\mathbb{1}, \tag{16}$$

where $\mathbb{1}$ is the identity matrix.

B. Static structure factor

We now calculate the equal time density correlation function in Fourier space, the static structure factor, defined by

$$S(\boldsymbol{q}) = \frac{1}{N}\langle \delta\tilde{\rho}(\boldsymbol{q}, 0)\delta\tilde{\rho}^*(\boldsymbol{q}, 0)\rangle, \tag{17}$$

where $*$ represents the complex conjugate, and $\tilde{X}(\boldsymbol{q}, t)$ denotes the Fourier transform of $X(\boldsymbol{r}, t)$ with respect to $\boldsymbol{r}$: $\tilde{X}(\boldsymbol{q}, t) = \int_V \mathrm{d}^3\boldsymbol{r}\, X(\boldsymbol{r}, t)e^{-i\boldsymbol{q}\cdot\boldsymbol{r}}$. We also write the spatiotemporal Fourier transform of $X(\boldsymbol{r}, t)$ as $\hat{X}(\boldsymbol{q}, \omega) = \int_{-\infty}^{\infty} \mathrm{d}t\, \tilde{X}(\boldsymbol{q}, t)e^{i\omega t}$. In Fourier space, Eqs. (12) and (13) read

$$\mathsf{G}^{-1}(\boldsymbol{q}, \omega)\hat{\boldsymbol{\Phi}}(\boldsymbol{q}, \omega) = \hat{\boldsymbol{\Xi}}(\boldsymbol{q}, \omega), \tag{18}$$

where we define $\boldsymbol{\Phi}(\boldsymbol{r}, t) = [\rho(\boldsymbol{r}, t), \boldsymbol{p}(\boldsymbol{r}, t)]$, $\boldsymbol{\Xi}(\boldsymbol{r}, t) = \sqrt{4D\rho/3}[0, \boldsymbol{\Upsilon}(\boldsymbol{r}, t)]$, and

$$\mathsf{G}^{-1}(\boldsymbol{q}, \omega) = \begin{pmatrix} -i\omega + bq^2 & iv_0q_x & iv_0q_y & iv_0q_z \\ 0 & -i\omega + 2D & \Omega_z & -\Omega_y \\ 0 & -\Omega_z & -i\omega + 2D & \Omega_x \\ 0 & \Omega_y & -\Omega_x & -i\omega + 2D \end{pmatrix}. \tag{19}$$

The dynamical correlation functions in $(\boldsymbol{q}, \omega)$ space can be calculated as

$$\begin{aligned} S_{a,b}(\boldsymbol{q}, \omega) &:= \frac{1}{N}\int_{-\infty}^{\infty} \mathrm{d}t\, \langle \tilde{\Phi}_a(\boldsymbol{q}, t)\tilde{\Phi}_b^*(\boldsymbol{q}, 0)\rangle e^{i\omega t} \\ &= \frac{4D}{3}\sum_{c=2}^{4} G_{a,c}(\boldsymbol{q}, \omega)G_{b,c}^*(\boldsymbol{q}, \omega). \end{aligned} \tag{20}$$

Using this formula, the dynamical structure factor, $S(\boldsymbol{q}, \omega) := S_{1,1}(\boldsymbol{q}, \omega)$, ends up with

$$S(\boldsymbol{q}, \omega) = \frac{4v_0^2D}{3}\frac{q^2\omega^4 + [(8D^2+\Omega^2)q^2 - 3(\boldsymbol{\Omega}\cdot\boldsymbol{q})^2]\omega^2 + (4D^2+\Omega^2)[4D^2q^2 + (\boldsymbol{\Omega}\cdot\boldsymbol{q})^2]}{(\omega^2 + b^2q^4)(\omega^2 + 4D^2)\left[\{\omega^2 - (4D^2+\Omega^2)\}^2 + 16D^2\omega^2\right]}. \tag{21}$$

The static structure factor, Eq. (17), is obtained by integrating Eq. (21) over ω as

$$S(\boldsymbol{q}) = \frac{1}{2\pi}\int_{-\infty}^{\infty} \mathrm{d}\omega\, S(\boldsymbol{q}, \omega) = \frac{v_0^2}{3}\frac{q^2(2D + bq^2)^2 + (\boldsymbol{\Omega}\cdot\boldsymbol{q})^2}{bq^2(bq^2 + 2D)[(bq^2 + 2D)^2 + \Omega^2]}. \tag{22}$$

We first discuss the limit $D \to 0$, or equivalently, the infinite persistence time limit $\tau_{\rm p} = 1/(2D) \to \infty$. Equation (22) in this limit reduces to

$$S(\boldsymbol{q}) = \frac{v_0^2}{3}\frac{b^2q^6 + \Omega^2q_z^2}{b^2q^4(b^2q^4 + \Omega^2)}, \tag{23}$$

where the torque vector is chosen to be parallel to the z direction as $\boldsymbol{\Omega} = (0, 0, \Omega)$. Figures 3(b) and 3(d) depict contour plots of Eq. (23) on the q_x-q_z and q_x-q_y planes, respectively. The static structure factor exhibits an anisotropic shape in the q_x-q_z plane, while it appears isotropic in the q_x-q_y plane. These behaviors are qualitatively in agreement with the numerical observations shown in Figs. 3(a) and 3(c). Furthermore, $S(\boldsymbol{q})$ has a singularity at the origin, as indicated by the numerical simulation in the previous section. To see the singularity, we focus on the behavior on the q_z and q_x axes. Along the q_z axis, Eq. (23) reduces to

$$S(0, 0, q_z) = \frac{v_0^2}{3b^2}\frac{1}{q_z^2}, \tag{24}$$

meaning that the density fluctuations increase at large scales for the z direction. In contrast, along the q_x axis, $S(\boldsymbol{q})$ becomes

$$S(q_x, 0, 0) = \frac{v_0^2}{3}\frac{q_x^2}{\Omega^2 + b^2q_x^4} = \frac{1}{3}(Rq_x)^2 + O\big(q_x^6\big), \tag{25}$$

where $R = v_0/\Omega$. Equation (25) is a scaling of hyperuniformity with the exponent $\alpha = 2$, which is identical to that of two-dimensional cABP [18,29]. Therefore, Eq. (23) is singular at the origin $\lim_{q_z\to 0} S(0, 0, q_z) \neq \lim_{q_x\to 0} S(q_x, 0, 0)$. This singular behavior is also consistent with the numerical observations. However, the exponent of $S(0, 0, q_z)$ disagrees with the numerical result. The static structure factor $S(0, 0, q_z)$ obtained from the numerical simulation shown in Fig. 4(a) is $S(0, 0, q_z) \sim 1/q_z$, in contrast to the theoretical prediction $S(0, 0, q_z) \propto 1/q_z^2$. Moreover, this scaling appears to terminate around $q_z = 0.4$, suggesting the existence of a characteristic length scale, whereas the theory predicts a scale-free behavior. We remark that the characteristic length scale observed in the numerically obtained $S(0, 0, q_z)$ in Fig. 4(a) is not attributable to finite-size structures, as there is no sign of clustering or phase separation (see Fig. 2). Since our particle model can be effectively regarded as "one-dimensional ABP" along the z-axis, one possible reason for this discrepancy is the

presence of anomalies specific to one-dimensional systems, such as single-file diffusion [98], which are not captured by our theory. Another possibility is the different behavior of the correlation length in one-dimensional ABP. It has been reported that, in a narrow annular confinement, the correlation length saturates to a constant value as the persistence time $\tau_{\rm p}$ increases [99], whereas the correlation length in two dimensions is proportional to $\sqrt{\tau_{\rm p}}$ [80–82]. This effect is also beyond the scope of our theory. In contrast, the theoretical prediction of the hyperuniform exponent in $S(q_x, 0, 0)$ agrees with the numerical data. However, the theoretical expression for $S(q_x, 0, 0)$, Eq. (25), is not fully quantitative, that is, a discrepancy in the prefactor remains. The dash-dotted lines in Fig. 4(b) depict the theoretical predictions Eq. (25). The parameter b is determined by the fitting but does not affect the hyperuniform scaling, as is obvious in the second equation in Eq. (25). The theoretical line for $R = 1$ deviates from the numerical data, while for $R = 3$ the agreement is somewhat better. As for $R = 10$ and 100, we cannot discuss quantitative assessment with the current system size. Further theoretical calculations, such as nonlinear analysis, would be required for a quantitative description.

Finally, we discuss the case of finite rotational diffusion constants D. On the q_z and q_x axis, Eq. (23) is written as

$$S(0, 0, q_z) = \frac{S_0}{1 + (\xi q_z)^2}, \tag{26}$$

$$S(q_x, 0, 0) = \frac{v_0^2}{3b} \frac{2D + bq_x^2}{\Omega^2 + (bq_x^2 + 2D)^2}, \tag{27}$$

respectively. Here $S_0 := v_0^2/(6bD)$ and $\xi := \sqrt{b/(2D)}$. Both on the q_z and q_x axes, $S(\boldsymbol{q} \to \boldsymbol{0})$ remains constant, but $S(\boldsymbol{q})$ is still singular at the origin. To measure how strong the singularity is, depending on the parameters D and Ω, we introduce the following ratio [70]:

$$\mathcal{R} := \frac{\lim_{q_z \to 0} S(0, 0, q_z)}{\lim_{q_x \to 0} S(q_x, 0, 0)} = 1 + \frac{\Omega^2}{4D^2} = 1 + (\Omega \tau_{\rm p})^2, \tag{28}$$

where we use $\tau_{\rm p} = 1/(2D)$ in the last equality. This ratio becomes unity either when $\Omega = 0$ or in the limit $D \to \infty$. In the former case, the system reduces to three-dimensional ABP without chirality [74–77], and the static structure factor takes the Ornstein-Zernike form $S(q) = S_0/[1 + (\xi q)^2]$. In the latter case, corresponding to the equilibrium limit, the structure factor becomes a constant, $S(q) = S_0 = \rho T_{\rm act} \chi$, which is a well-known expression of $S(q \to 0)$ in equilibrium statistical mechanics [100]. Except in these two cases, $\mathcal{R}$ is not unity. Increasing Ω or decreasing D renders the singularity stronger. In particular, $\mathcal{R}$ diverges in the limit $D \to 0$ or $\tau_{\rm p} \to \infty$. This behavior stands in contrast to anisotropic active fluids and driven lattice gases, in which $\mathcal{R}$ remains finite [66,67,69,70].

V. SUMMARY

In this paper, we studied density fluctuations in a three-dimensional chiral active fluid using a helical self-propelled particle model. We considered a simple situation where all the particles have the same torque and perform a helical motion with a persistence time. Extensive numerical simulations of the model revealed that the static structure factor in homogeneous states showed an anisotropic pattern and is singular at the origin in Fourier space. These features resemble those observed in other anisotropic nonequilibrium fluids, such as anisotropic active fluids [66–68] and driven diffusive gases [69,70]. Moreover, in the limit of large persistence time, the system exhibits hyperuniformity in the direction perpendicular to the torque, while showing giant density fluctuations in the direction parallel to it. To understand the numerical observations, we developed an effective fluctuating hydrodynamic theory for homogeneous fluid states of 3D cABP. The theory successfully reproduces the same qualitative behavior of the density correlation functions as observed in numerical simulations, although it does not achieve full quantitative agreement.

As a future direction, it is important to investigate the full phase behavior of three-dimensional chiral active particles. In two dimensions, chiral active particles are known to exhibit clustering [14,18,73,87], and it is therefore natural to expect similar behavior in three dimensions. Moreover, two-dimensional chiral active particles can crystallize with long-range translational order [20], suggesting that chirality may also play a significant role in crystallization in three dimensions. In addition, while the present study assumes identical torques for all particles, exploring the effects of torque dispersion would be an important extension.

From an experimental perspective, singular density correlations found in the present study may be challenging to observe but could become accessible in future experiments, especially given that hyperuniformity in two-dimensional chiral active fluids has already been observed experimentally using swimming marine algae [27] and pear-shaped Quincke rollers [28]. For example, the marine algae used in Ref. [27] might also be suitable for studying the three-dimensional case, as they are known to exhibit helical trajectories when they are far from interfaces. Additionally, bottom-heavy Janus particles swimming in three-dimensional space [101,102] and magnetically driven particles [103] could serve as potential experimental systems for investigating density correlations in three-dimensional chiral active fluids.

ACKNOWLEDGMENTS

Y.K. acknowledges support by JSPS KAKENHI (Grant No. JP23KJ1068). T.K. acknowledges support by the JST FOREST Program (Grant No. JPMJFR212T), AMED Moonshot Program (Grant No. JP22zf0127009), JSPS KAKENHI (Grant No. JP24H02203), and Takeda Science Foundation. K.M. acknowledges support by JSPS KAKENHI (Grant No. JP24H00192).

DATA AVAILABILITY

The data that support the findings of this article are openly available [104].

APPENDIX: DERIVATION OF FLUCTUATING HYDRODYNAMIC EQUATIONS

In this Appendix, we derive the fluctuating hydrodynamic equations by extending Dean's method [93,94] to 3D cABP.

1. Derivation of Eqs. (7) and (8)

First, we derive the equation for the density field. The time derivative of Eq. (4) leads to the continuity equation as

$$\partial_t \rho(\boldsymbol{r},t) = -\nabla\cdot\boldsymbol{J}(\boldsymbol{r},t), \tag{A1}$$

where the density current $\boldsymbol{J}(\boldsymbol{r},t)$ is given by

$$\begin{aligned}\boldsymbol{J}(\boldsymbol{r},t) &:= \sum_{j=1}^{N}\dot{\boldsymbol{r}}_j(t)\delta[\boldsymbol{r}-\boldsymbol{r}_j(t)]\\ &= \mu\sum_{j=1}^{N}\boldsymbol{F}_j(t)\delta[\boldsymbol{r}-\boldsymbol{r}_j(t)] + v_0\boldsymbol{p}(\boldsymbol{r},t).\end{aligned} \tag{A2}$$

The first term of Eq. (A2) can be rewritten as

$$\sum_{j=1}^{N}\boldsymbol{F}_j(t)\delta[\boldsymbol{r}-\boldsymbol{r}_j(t)] = -\rho(\boldsymbol{r},t)\nabla\frac{\delta\mathcal{F}[\rho(\cdot,t)]}{\delta\rho(\boldsymbol{r},t)}. \tag{A3}$$

The functional $\mathcal{F}[\rho]$ is defined by Eq. (10), and Eq. (A3) can be interpreted as the divergence of the "pressure" tensor as in Eq. (9). We next construct the equation for the polarization defined in Eq. (5). Taking the time derivative of Eq. (5), we get

$$\partial_t\boldsymbol{p}(\boldsymbol{r},t) = -\nabla\cdot\mathsf{M}(\boldsymbol{r},t) + \sum_{j=1}^{N}\frac{\mathrm{d}\boldsymbol{e}_j(t)}{\mathrm{d}t}\delta[\boldsymbol{r}-\boldsymbol{r}_j(t)], \tag{A4}$$

where the tensor $\mathsf{M}(\boldsymbol{r},t)$ is defined as

$$\mathsf{M}(\boldsymbol{r},t) := \sum_{j=1}^{N}\dot{\boldsymbol{r}}_j(t)\boldsymbol{e}_j(t)\delta[\boldsymbol{r}-\boldsymbol{r}_j(t)]. \tag{A5}$$

To express Eq. (A5) in terms of the hydrodynamic fields, we assume that

$$\delta[\boldsymbol{r}_j(t)-\boldsymbol{r}_k(t)] = \delta[\boldsymbol{r}_j(t)-\boldsymbol{r}_k(t)]\delta_{j,k}, \tag{A6}$$

following Ref. [94]. This relation is correct if the particles j and k never occupy the same position simultaneously, such as when the pairwise potential $U(r)$ is the repulsive interaction [94]. With the assumption Eq. (A6), Eq. (A5) can be written as

$$\mathsf{M}(\boldsymbol{r},t) = \frac{\boldsymbol{J}(\boldsymbol{r},t)\boldsymbol{p}(\boldsymbol{r},t)}{\rho(\boldsymbol{r},t)}. \tag{A7}$$

To rewrite the last term on the RHS of Eq. (A4), we use Eq. (2) in the Itô representaion [71]

$$\frac{\mathrm{d}\boldsymbol{e}_j(t)}{\mathrm{d}t} = -2D\boldsymbol{e}_j(t) + (\boldsymbol{\Omega}+\sqrt{2D}\boldsymbol{\eta}_j(t))\overset{\mathrm{i}}{\times}\boldsymbol{e}_j(t), \tag{A8}$$

where the symbol $\overset{\mathrm{i}}{\times}$ means that the cross product is taken in the Itô sense. By substituting Eqs. (A7) and (A8) into Eq. (A4), we have

$$\begin{aligned}\partial_t\boldsymbol{p}(\boldsymbol{r},t) =& -\nabla\cdot\left(\frac{\boldsymbol{J}(\boldsymbol{r},t)\boldsymbol{p}(\boldsymbol{r},t)}{\rho(\boldsymbol{r},t)}\right) - 2D\boldsymbol{p}(\boldsymbol{r},t)\\ &+\boldsymbol{\Omega}\times\boldsymbol{p}(\boldsymbol{r},t) + \boldsymbol{\Lambda}(\boldsymbol{r},t),\end{aligned} \tag{A9}$$

where $\boldsymbol{\Lambda}(\boldsymbol{r},t)$ is defined by

$$\boldsymbol{\Lambda}(\boldsymbol{r},t) := \sqrt{2D}\sum_{j=1}^{N}\boldsymbol{\eta}_j(t)\overset{\mathrm{i}}{\times}\boldsymbol{e}_j(t)\delta[\boldsymbol{r}-\boldsymbol{r}_j(t)]. \tag{A10}$$

Equation (A10) is not closed for the hydrodynamic fields but can be written as the following simple form in the large N limit

$$\boldsymbol{\Lambda}(\boldsymbol{r},t) = \sqrt{\frac{4D\rho(\boldsymbol{r},t)}{3}}\boldsymbol{\Upsilon}(\boldsymbol{r},t), \tag{A11}$$

where $\boldsymbol{\Upsilon}(\boldsymbol{r},t)$ is a Gaussian white noise with zero mean and correlation $\langle\Upsilon_\alpha(\boldsymbol{r},t)\Upsilon_\beta(\boldsymbol{r}',t')\rangle = \delta_{\alpha,\beta}\delta(\boldsymbol{r}-\boldsymbol{r}')\delta(t-t')$. We thus reach Eqs. (6) to (8) aside from the derivation of Eq. (A11).

2. Justification of Eq. (A11)

Here, we show that the expectation value and the two-point correlation of Eq. (A10) are identical to those of Eq. (A11) in the large N limit. First, the expectation value of Eq. (A10) is obviously zero since the cross product is taken in the Itô representation. Next, the correlation between the elements α and β of Eq. (A10) is

$$\begin{aligned}\langle\Lambda_\alpha(\boldsymbol{r},t)\Lambda_\beta(\boldsymbol{r}',t')\rangle =& 2D\sum_{j=1}^{N}\delta(t-t')\delta(\boldsymbol{r}-\boldsymbol{r}')\delta[\boldsymbol{r}-\boldsymbol{r}_j(t)]\\ &\times\sum_{\mu,\nu,\sigma\in\{x,y,z\}}\epsilon_{\alpha\mu\nu}\epsilon_{\beta\mu\sigma}\left\langle e_j^{(\nu)}(t)e_j^{(\sigma)}(t)\right\rangle.\end{aligned} \tag{A12}$$

To estimate this correlation, we calculate the autocorrelation function $\langle e_j^{(\alpha)}(t)e_j^{(\beta)}(t)\rangle$. Using the Itô formula [71], one can derive the differential equation for this autocorrelation function

$$\begin{aligned}\frac{\mathrm{d}}{\mathrm{d}t}\left\langle e_j^{(\alpha)}(t)e_j^{(\beta)}(t)\right\rangle =& -6D\left[\left\langle e_j^{(\alpha)}(t)e_j^{(\beta)}(t)\right\rangle - \frac{1}{3}\delta_{\alpha,\beta}\right]\\ &+\sum_{\mu,\nu}\left[\epsilon_{\alpha\mu\nu}\left\langle e_j^{(\beta)}(t)e_j^{(\nu)}(t)\right\rangle\right.\\ &\left.+\epsilon_{\beta\mu\nu}\left\langle e_j^{(\alpha)}(t)e_j^{(\nu)}(t)\right\rangle\right]\Omega_\mu.\end{aligned} \tag{A13}$$

By introducing a symmetric matrix

$$\mathsf{Q}_j(t) := \left\langle\boldsymbol{e}_j(t)\boldsymbol{e}_j^{\mathrm{T}}(t)\right\rangle - \tfrac{1}{3}\mathbb{1} \tag{A14}$$

and an antisymmetric matrix

$$H_{\alpha,\beta} := \sum_{\mu}\Omega_\mu\epsilon_{\alpha\mu\beta}, \tag{A15}$$

Eq. (A13) can be written as

$$\frac{\mathrm{d}}{\mathrm{d}t}\mathsf{Q}_j(t) = -\zeta\mathsf{Q}_j(t) + [\mathsf{H},\mathsf{Q}_j(t)], \tag{A16}$$

where $\zeta := 6D$ and $[\mathsf{X},\mathsf{Y}] := \mathsf{XY}-\mathsf{YX}$ denotes the commutator. Equation (A16) is the same form as the Heisenberg equation with a dissipation in imaginary time. The formal solution of Eq. (A16) is given by

$$\mathsf{Q}_j(t) = e^{-\zeta t}e^{t\mathsf{H}}\mathsf{Q}_j(0)e^{-t\mathsf{H}}. \tag{A17}$$

We now define

$$\mathcal{Q}^{(N)}_{\alpha,\beta}(\boldsymbol{r},t) := \sum_{j=1}^{N} Q_j^{(\alpha,\beta)}(0)\delta[\boldsymbol{r}-\boldsymbol{r}_j(t)] \tag{A18}$$

and evaluate this quantity in the large N limit. Here, $Q_j^{(\alpha,\beta)}(0)$ is an element of the matrix $\mathsf{Q}_j(0)$ in Eq. (A17). We assume that the initial orientation $\boldsymbol{e}_j(0)$ is chosen uniformly at random on the unit sphere. Then

$$\lim_{N\to\infty}\frac{1}{N}\sum_{j=1}^{N} Q_j^{(\alpha,\beta)}(0) = \frac{1}{4\pi}\int_{|\boldsymbol{e}|=1} \mathrm{d}^3\boldsymbol{e}\left(e_\alpha e_\beta - \frac{1}{3}\delta_{\alpha,\beta}\right) = 0. \tag{A19}$$

To evaluate Eq. (A18), we expand it in a Fourier series

$$\mathcal{Q}^{(N)}_{\alpha,\beta}(\boldsymbol{r},t) = \sum_{\boldsymbol{n}\in\mathbb{Z}^3} \widetilde{\mathcal{Q}}^{(N)}_{\alpha,\beta}(\boldsymbol{n},t)e^{2\pi i\boldsymbol{n}\cdot\boldsymbol{r}/L}, \tag{A20}$$

where the Fourier coefficient is given by

$$\widetilde{\mathcal{Q}}^{(N)}_{\alpha,\beta}(\boldsymbol{n},t) = \frac{1}{L^3}\sum_{j=1}^{N} Q_j^{(\alpha,\beta)}(0)e^{-2\pi i\boldsymbol{n}\cdot\boldsymbol{r}_j/L}. \tag{A21}$$

Since $\sum_{j=1}^{N} Q_j^{(\alpha,\beta)}(0) = o(N) = o(L^3)$ from Eq. (A19), we have

$$\left|\widetilde{\mathcal{Q}}^{(N)}_{\alpha,\beta}(\boldsymbol{n},t)\right| \leqslant \frac{1}{L^3}\left|\sum_{j=1}^{N} Q_j^{(\alpha,\beta)}(0)\right| = o(1). \tag{A22}$$

Thus, Eq. (A18) converges to zero in the large N limit

$$\lim_{N\to\infty}\mathcal{Q}^{(N)}_{\alpha,\beta}(\boldsymbol{r},t) = 0. \tag{A23}$$

Using Eqs. (A14), (A17), and (A23), we obtain

$$\sum_{j=1}^{N}\left\langle e_j^{(\alpha)}(t)e_j^{(\beta)}(t)\right\rangle\delta(\boldsymbol{r}-\boldsymbol{r}_j) = \frac{\rho(\boldsymbol{r},t)}{3}\delta_{\alpha,\beta} + o(1) \tag{A24}$$

in the limit $N\to\infty$. Therefore, Eq. (A12) in the limit $N\to\infty$ reads

$$\langle\Lambda_\alpha(\boldsymbol{r},t)\Lambda_\beta(\boldsymbol{r}',t')\rangle = \frac{4D}{3}\rho(\boldsymbol{r},t)\delta_{\alpha,\beta}\delta(\boldsymbol{r}-\boldsymbol{r}')\delta(t-t') + o(1). \tag{A25}$$

This means that $\boldsymbol{\Lambda}(\boldsymbol{r},t)$ in Eqs. (A10) and (A11) is statistically identical, at least up to the second cumulant.

[1] S. Ramaswamy, The mechanics and statistics of active matter, Annu. Rev. Condens. Matter Phys. **1**, 323 (2010).

[2] C. Bechinger, R. Di Leonardo, H. Löwen, C. Reichhardt, G. Volpe, and G. Volpe, Active particles in complex and crowded environments, Rev. Mod. Phys. **88**, 045006 (2016).

[3] A. Zöttl and H. Stark, Modeling active colloids: From active Brownian particles to hydrodynamic and chemical fields, Annu. Rev. Condens. Matter Phys. **14**, 109 (2023).

[4] H. Löwen, Chirality in microswimmer motion: From circle swimmers to active turbulence, Eur. Phys. J.: Spec. Top. **225**, 2319 (2016).

[5] B. Liebchen and D. Levis, Chiral active matter, Europhys. Lett. **139**, 67001 (2022).

[6] F. Kümmel, B. ten Hagen, R. Wittkowski, I. Buttinoni, R. Eichhorn, G. Volpe, H. Löwen, and C. Bechinger, Circular motion of asymmetric self-propelling particles, Phys. Rev. Lett. **110**, 198302 (2013).

[7] B. Zhang, A. Sokolov, and A. Snezhko, Reconfigurable emergent patterns in active chiral fluids, Nat. Commun. **11**, 4401 (2020).

[8] T. Mano, J.-B. Delfau, J. Iwasawa, and M. Sano, Optimal run-and-tumble–based transportation of a Janus particle with active steering, Proc. Natl. Acad. Sci. USA **114**, 2580 (2017).

[9] I. H. Riedel, K. Kruse, and J. Howard, A self-organized vortex array of hydrodynamically entrained sperm cells, Science **309**, 300 (2005).

[10] P. Patra, K. Beyer, A. Jaiswal, A. Battista, K. Rohr, F. Frischknecht, and U. S. Schwarz, Collective migration reveals mechanical flexibility of malaria parasites, Nat. Phys. **18**, 586 (2022).

[11] W. R. DiLuzio, L. Turner, M. Mayer, P. Garstecki, D. B. Weibel, H. C. Berg, and G. M. Whitesides, Escherichia coli swim on the right-hand side, Nature (London) **435**, 1271 (2005).

[12] R. Di Leonardo, D. Dell'Arciprete, L. Angelani, and V. Iebba, Swimming with an image, Phys. Rev. Lett. **106**, 038101 (2011).

[13] F. Siebers, A. Jayaram, P. Blümler, and T. Speck, Exploiting compositional disorder in collectives of light-driven circle walkers, Sci. Adv. **9**, eadf5443 (2023).

[14] B. Liebchen and D. Levis, Collective behavior of chiral active matter: Pattern formation and enhanced flocking, Phys. Rev. Lett. **119**, 058002 (2017).

[15] N. Kruk, J. A. Carrillo, and H. Koeppl, Traveling bands, clouds, and vortices of chiral active matter, Phys. Rev. E **102**, 022604 (2020).

[16] B. Ventejou, H. Chaté, R. Montagne, and X. Q. Shi, Susceptibility of orientationally ordered active matter to chirality disorder, Phys. Rev. Lett. **127**, 238001 (2021).

[17] G.-J. Liao and S. H. L. Klapp, Emergent vortices and phase separation in systems of chiral active particles with dipolar interactions, Soft Matter **17**, 6833 (2021).

[18] Q.-L. Lei, M. P. Ciamarra, and R. Ni, Nonequilibrium strongly hyperuniform fluids of circle active particles with large local density fluctuations, Sci. Adv. **5**, eaau7423 (2019).

[19] V. E. Debets, H. Löwen, and L. M. C. Janssen, Glassy dynamics in chiral fluids, Phys. Rev. Lett. **130**, 058201 (2023).

[20] Y. Kuroda, T. Kawasaki, and K. Miyazaki, Long-range translational order and hyperuniformity in two-dimensional chiral active crystal, Phys. Rev. Res. **7**, L012048 (2025).

[21] K. Jeong, Y. Kuroda, Y. Asatani, T. Kawasaki, and K. Miyazaki, Crystallization of chiral active Brownian particles at low densities, Phys. Rev. Res. (2025), doi:10.1103/yntx-ss9r.

[22] F. Siebers, R. Bebon, A. Jayaram, and T. Speck, Collective Hall current in chiral active fluids: Coupling of phase and mass transport through traveling bands, Proc. Natl. Acad. Sci. USA **121**, e2320256121 (2024).

[23] L. Caprini, B. Liebchen, and H. Löwen, Self-reverting vortices in chiral active matter, Commun. Phys. **7**, 153 (2024).

[24] J. L. Aragones, J. P. Steimel, and A. Alexander-Katz, Elasticity-induced force reversal between active spinning particles in dense passive media, Nat. Commun. **7**, 11325 (2016).
[25] V. Soni, E. S. Bililign, S. Magkiriadou, S. Sacanna, D. Bartolo, M. J. Shelley, and W. T. M. Irvine, The odd free surface flows of a colloidal chiral fluid, Nat. Phys. **15**, 1188 (2019).
[26] T. H. Tan, A. Mietke, J. Li, Y. Chen, H. Higinbotham, P. J. Foster, S. Gokhale, J. Dunkel, and N. Fakhri, Odd dynamics of living chiral crystals, Nature (London) **607**, 287 (2022).
[27] M. Huang, W. Hu, S. Yang, Q.-X. Liu, and H. P. Zhang, Circular swimming motility and disordered hyperuniform state in an algae system, Proc. Natl. Acad. Sci. USA **118**, e2100493118 (2021).
[28] B. Zhang and A. Snezhko, Hyperuniform active chiral fluids with tunable internal structure, Phys. Rev. Lett. **128**, 218002 (2022).
[29] Y. Kuroda and K. Miyazaki, Microscopic theory for hyperuniformity in two-dimensional chiral active fluid, J. Stat. Mech.: Theory Exp. (2023) 103203.
[30] S. Torquato, Hyperuniform states of matter, Phys. Rep. **745**, 1 (2018).
[31] Y. Lei and R. Ni, Non-equilibrium dynamic hyperuniform states, J. Phys.: Condens. Matter **37**, 023004 (2025).
[32] S. Ramaswamy, R. A. Simha, and J. Toner, Active nematics on a substrate: Giant number fluctuations and long-time tails, Europhys. Lett. **62**, 196 (2003).
[33] V. Narayan, S. Ramaswamy, and N. Menon, Long-Lived giant number fluctuations in a swarming granular nematic, Science **317**, 105 (2007).
[34] H. P. Zhang, A. Be'er, E. L. Florin, and H. L. Swinney, Collective motion and density fluctuations in bacterial colonies, Proc. Natl. Acad. Sci. USA **107**, 13626 (2010).
[35] D. Nishiguchi, K. H. Nagai, H. Chaté, and M. Sano, Long-range nematic order and anomalous fluctuations in suspensions of swimming filamentous bacteria, Phys. Rev. E **95**, 020601(R) (2017).
[36] J. Iwasawa, D. Nishiguchi, and M. Sano, Algebraic correlations and anomalous fluctuations in ordered flocks of Janus particles fueled by an AC electric field, Phys. Rev. Res. **3**, 043104 (2021).
[37] H. Chaté, F. Ginelli, and R. Montagne, Simple model for active nematics: Quasi-long-range order and giant fluctuations, Phys. Rev. Lett. **96**, 180602 (2006).
[38] H. Chaté, F. Ginelli, G. Grégoire, and F. Raynaud, Collective motion of self-propelled particles interacting without cohesion, Phys. Rev. E **77**, 046113 (2008).
[39] F. Ginelli, F. Peruani, M. Bär, and H. Chaté, Large-scale collective properties of self-propelled rods, Phys. Rev. Lett. **104**, 184502 (2010).
[40] K. Kawaguchi, R. Kageyama, and M. Sano, Topological defects control collective dynamics in neural progenitor cell cultures, Nature (London) **545**, 327 (2017).
[41] J. H. Weijs, R. Jeanneret, R. Dreyfus, and D. Bartolo, Emergent hyperuniformity in periodically driven emulsions, Phys. Rev. Lett. **115**, 108301 (2015).
[42] E. Tjhung and L. Berthier, Hyperuniform density fluctuations and diverging dynamic correlations in periodically driven colloidal suspensions, Phys. Rev. Lett. **114**, 148301 (2015).
[43] D. Hexner and D. Levine, Hyperuniformity of critical absorbing states, Phys. Rev. Lett. **114**, 110602 (2015).
[44] D. Hexner and D. Levine, Noise, diffusion, and hyperuniformity, Phys. Rev. Lett. **118**, 020601 (2017).
[45] Q.-L. Lei and R. Ni, Hydrodynamics of random-organizing hyperuniform fluids, Proc. Natl. Acad. Sci. USA **116**, 22983 (2019).
[46] L. Galliano, M. E. Cates, and L. Berthier, Two-dimensional crystals far from equilibrium, Phys. Rev. Lett. **131**, 047101 (2023).
[47] H. Ikeda, Harmonic chain far from equilibrium: Single-file diffusion, long-range order, and hyperuniformity, SciPost Phys. **17**, 103 (2024).
[48] R. Maire, L. Galliano, A. Plati, and L. Berthier, Hyperuniform interfaces in non-equilibrium phase coexistence, arXiv:2507.03957.
[49] R. Maire and A. Plati, Enhancing (quasi-)long-range order in a two-dimensional driven crystal, J. Chem. Phys. **161**, 054902 (2024).
[50] R. Maire, A. Plati, F. Smallenburg, and G. Foffi, Dynamical and structural properties of an absorbing phase transition: a case study from granular systems, arXiv:2507.06083.
[51] J. Chen, X. Lei, Y. Xiang, M. Duan, X. Peng, and H. P. Zhang, Emergent chirality and hyperuniformity in an active mixture with nonreciprocal interactions, Phys. Rev. Lett. **132**, 118301 (2024).
[52] Z.-Q. Li, Q.-L. Lei, and Y.-Q. Ma, Fluidization and anomalous density fluctuations in 2D Voronoi cell tissues with pulsating activity, Proc. Natl. Acad. Sci. USA **122**, e2421518122 (2025).
[53] H.-H. Boltz and T. Ihle, Hyperuniformity in deterministic antialigning active matter, arXiv:2402.19451.
[54] Z. Ma and S. Torquato, Random scalar fields and hyperuniformity, J. Appl. Phys. **121**, 244904 (2017).
[55] Y. Zheng, M. A. Klatt, and H. Löwen, Universal hyperuniformity in active field theories, Phys. Rev. Res. **6**, L032056 (2024).
[56] J. F. Jikeli, L. Alvarez, B. M. Friedrich, L. G. Wilson, R. Pascal, R. Colin, M. Pichlo, A. Rennhack, C. Brenker, and U. B. Kaupp, Sperm navigation along helical paths in 3D chemoattractant landscapes, Nat. Commun. **6**, 7985 (2015).
[57] J. B. Kirkegaard, A. O. Marron, and R. E. Goldstein, Motility of colonial choanoflagellates and the statistics of aggregate random walkers, Phys. Rev. Lett. **116**, 038102 (2016).
[58] C. Krüger, G. Klös, C. Bahr, and C. C. Maass, Curling liquid crystal microswimmers: A cascade of spontaneous symmetry breaking, Phys. Rev. Lett. **117**, 048003 (2016).
[59] T. Yamamoto and M. Sano, Chirality-induced helical self-propulsion of cholesteric liquid crystal droplets, Soft Matter **13**, 3328 (2017).
[60] F. J. Sevilla, Diffusion of active chiral particles, Phys. Rev. E **94**, 062120 (2016).
[61] A. Pattanayak, A. Shee, D. Chaudhuri, and A. Chaudhuri, Impact of torque on active Brownian particle: Exact moments in two and three dimensions, New J. Phys. **26**, 083024 (2024).
[62] P. S. Burada, R. Maity, and F. Jülicher, Hydrodynamics of chiral squirmers, Phys. Rev. E **105**, 024603 (2022).

[63] M. Lisicki, S. Y. Reigh, and E. Lauga, Autophoretic motion in three dimensions, Soft Matter **14**, 3304 (2018).

[64] S. Rode, J. Elgeti, and G. Gompper, Multi-ciliated microswimmers–metachronal coordination and helical swimming, Eur. Phys. J. E **44**, 76 (2021).

[65] S. Samatas and J. Lintuvuori, Hydrodynamic synchronization of chiral microswimmers, Phys. Rev. Lett. **130**, 024001 (2023).

[66] K. Adachi, K. Takasan, and K. Kawaguchi, Activity-induced phase transition in a quantum many-body system, Phys. Rev. Res. **4**, 013194 (2022).

[67] H. Nakano and K. Adachi, Universal properties of repulsive self-propelled particles and attractive driven particles, Phys. Rev. Res. **6**, 013074 (2024).

[68] K. Adachi and H. Nakano, Power-law correlation in the homogeneous disordered state of anisotropically self-propelled systems, Phys. Rev. Res. **6**, 033234 (2024).

[69] B. Schmittmann and R. K. P. Zia, *Statistical Mechanics of Driven Diffusive System*, edited by B. Schmittmann and R. Zia, Phase Transitions and Critical Phenomena (Academic Press, New York, 1995), Vol. 17.

[70] B. Schmittmann and R. Zia, Driven diffusive systems. An introduction and recent developments, Phys. Rep. **301**, 45 (1998).

[71] C. Gardiner, *Stochastic Methods: A Handbook for the Natural and Social Sciences* (Springer, Berlin, 2009).

[72] Z. Ma, Q.-l. Lei, and R. Ni, Driving dynamic colloidal assembly using eccentric self-propelled colloids, Soft Matter **13**, 8940 (2017).

[73] Z. Ma and R. Ni, Dynamical clustering interrupts motility-induced phase separation in chiral active Brownian particles, J. Chem. Phys. **156**, 021102 (2022).

[74] A. Wysocki, R. G. Winkler, and G. Gompper, Cooperative motion of active Brownian spheres in three-dimensional dense suspensions, Europhys. Lett. **105**, 48004 (2014).

[75] J. Stenhammar, D. Marenduzzo, R. J. Allen, and M. E. Cates, Phase behavior of active Brownian particles: The role of dimensionality, Soft Matter **10**, 1489 (2014).

[76] T. F. F. Farage, P. Krinninger, and J. M. Brader, Effective interactions in active Brownian suspensions, Phys. Rev. E **91**, 042310 (2015).

[77] J. T. Siebert, J. Letz, T. Speck, and P. Virnau, Phase behavior of active Brownian disks, spheres, and dimers, Soft Matter **13**, 1020 (2017).

[78] J. D. Weeks, D. Chandler, and H. C. Andersen, Role of repulsive forces in determining the equilibrium structure of simple liquids, J. Chem. Phys. **54**, 5237 (1971).

[79] S. Torquato, Hyperuniformity and its generalizations, Phys. Rev. E **94**, 022122 (2016).

[80] L. Caprini, U. M. B. Marconi, C. Maggi, M. Paoluzzi, and A. Puglisi, Hidden velocity ordering in dense suspensions of self-propelled disks, Phys. Rev. Res. **2**, 023321 (2020).

[81] G. Szamel and E. Flenner, Long-ranged velocity correlations in dense systems of self-propelled particles, Europhys. Lett. **133**, 60002 (2021).

[82] Y. Kuroda, H. Matsuyama, T. Kawasaki, and K. Miyazaki, Anomalous fluctuations in homogeneous fluid phase of active Brownian particles, Phys. Rev. Res. **5**, 013077 (2023).

[83] G. Szamel and E. Flenner, Extremely persistent dense active fluids, Soft Matter **20**, 5237 (2024).

[84] J. Bialké, H. Löwen, and T. Speck, Microscopic theory for the phase separation of self-propelled repulsive disks, Europhys. Lett. **103**, 30008 (2013).

[85] T. Speck, A. M. Menzel, J. Bialké, and H. Löwen, Dynamical mean-field theory and weakly non-linear analysis for the phase separation of active Brownian particles, J. Chem. Phys. **142**, 224109 (2015).

[86] M. T. Vrugt, J. Bickmann, and R. Wittkowski, How to derive a predictive field theory for active Brownian particles: A step-by-step tutorial, J. Phys.: Condens. Matter **35**, 313001 (2023).

[87] J. Bickmann, S. Bröker, J. Jeggle, and R. Wittkowski, Analytical approach to chiral active systems: Suppressed phase separation of interacting Brownian circle swimmers, J. Chem. Phys. **156**, 194904 (2022).

[88] E. Sesé-Sansa, D. Levis, and I. Pagonabarraga, Microscopic field theory for structure formation in systems of self-propelled particles with generic torques, J. Chem. Phys. **157**, 224905 (2022).

[89] K. L. Kreienkamp and S. H. L. Klapp, Clustering and flocking of repulsive chiral active particles with non-reciprocal couplings, New J. Phys. **24**, 123009 (2022).

[90] E. Kalz, A. Sharma, and R. Metzler, Field theory of active chiral hard disks: a first-principles approach to steric interactions, J. Phys. A: Math. Theor. **57**, 265002 (2024).

[91] U. M. B. Marconi, L. Caprini, and A. Puglisi, Hydrodynamics of simple active liquids: the emergence of velocity correlations, New J. Phys. **23**, 103024 (2021).

[92] T. Speck, Critical behavior of active Brownian particles: Connection to field theories, Phys. Rev. E **105**, 064601 (2022).

[93] D. S. Dean, Langevin equation for the density of a system of interacting Langevin processes, J. Phys. A: Math. Gen. **29**, L613 (1996).

[94] T. Nakamura and A. Yoshimori, Derivation of the nonlinear fluctuating hydrodynamic equation from the underdamped Langevin equation, J. Phys. A: Math. Theor. **42**, 065001 (2009).

[95] P. Illien, The Dean–Kawasaki equation and stochastic density functional theory, Rep. Prog. Phys. **88**, 086601 (2025).

[96] J. H. Irving and J. G. Kirkwood, The statistical mechanical theory of transport processes. IV. The equations of hydrodynamics, J. Chem. Phys. **18**, 817 (1950).

[97] M. Krüger, A. Solon, V. Démery, C. M. Rohwer, and D. S. Dean, Stresses in non-equilibrium fluids: Exact formulation and coarse-grained theory, J. Chem. Phys. **148**, 084503 (2018).

[98] A. Akintunde, P. Bayati, H. Row, and S. A. Mallory, Single-file diffusion of active Brownian particles, J. Chem. Phys. **162**, 164902 (2025).

[99] L. Caprini, C. Maggi, and U. Marini Bettolo Marconi, Collective effects in confined active Brownian particles, J. Chem. Phys. **154**, 244901 (2021).

[100] J. Hansen and I. McDonald, *Theory of Simple Liquids: With Applications to Soft Matter* (Elsevier Science, Amsterdam, 2013).

[101] A. I. Campbell and S. J. Ebbens, Gravitaxis in spherical Janus swimming devices, Langmuir **29**, 14066 (2013).

[102] A. I. Campbell, R. Wittkowski, B. ten Hagen, H. Löwen, and S. J. Ebbens, Helical paths, gravitaxis, and separation phenomena for mass-anisotropic self-propelling colloids: Experiment versus theory, J. Chem. Phys. **147**, 084905 (2017).

[103] P. Chen, S. Weady, S. Atis, T. Matsuzawa, M. J. Shelley, and W. T. M. Irvine, Self-propulsion, flocking and chiral active phases from particles spinning at intermediate Reynolds numbers, Nat. Phys. **21**, 146 (2025).

[104] https://doi.org/10.5281/zenodo.17241375.